J. Electrochem. Sci. Eng. **16** (2026) 3441; https://doi.org/10.5599/jese.3441

Open Access : : ISSN 1847-9286
https://pub.iapchem.org/ojs/index.php/JESE

Original scientific paper

Synthesis and characterization of an inorganic-organic nanomaterial for use as corrosion inhibitor for mild steel in HCl

Msenhemba Moses Mchihi[1,✉], Isioma Scholastica Odiachi[2], Adeola Praise Adeoti[2], Williams Jesse Adamu[1], Audu Ogbe Daniel[1,]

[1]*Department of Chemical Science, School of Science, Yaba College of Technology Lagos, Nigeria*
[2]*Department of Science Laboratory Technology, School of Science, Yaba College of Technology Lagos, Nigeria*

Corresponding Authors: ✉*mosesmsenhemba@gmail.com*; Tel: +2348125673784

Received: May 16, 2026; Accepted: June 24, 2026; Published: June 30, 2026

Abstract

The study of corrosion inhibitors for mild steel in HCl is crucial for enhancing the service life of industrial infrastructure, especially in environments prone to rapid deterioration and high maintenance costs. In this work, a zinc acetate-omeprazole nanomaterial (ZO) was prepared and its corrosion inhibition performance on mild steel deterioration in 0.5 M HCl solution was investigated using electrochemical techniques. The particles of the nano-material (with sizes ranging from 2.70 to 6.37 nm) predominantly exhibited a spherical to near-spherical morphology, with relatively smooth, well-defined edges. The mean hydrodynamic diameter of particles (Z-average diameter) of 59.79 nm indicates that the particles are primarily in the nanoscale range. The X-ray diffraction pattern of ZO revealed distinct diffraction peaks superimposed on a broad background, indicating the coexistence of crystalline and amorphous phases. A decrease in corrosion current density from 1781 μA cm^{-2} in the uninhibited medium to 1315 μA cm^{-2} upon the introduction of 0.1 g L^{-1} of ZO was observed. A progressive decline in corrosion current density was observed as inhibitor concentration increased. The shifts in corrosion potential were relatively small, suggesting that the inhibitor exhibits a mixed-type inhibition mechanism rather than a purely anodic or cathodic one. The charge transfer resistance increased from 210.21 Ω cm^2 in the absence of ZO to 230 Ω cm^2 in its presence (0.1 g L^{-1}). The electrochemical impedance spectroscopy results indicated that the highest inhibition efficiency achieved in this study was 77.6 % at 0.4 g L^{-1} ZO concentration. The inhibition efficiency increased with increasing inhibitor concentration. These findings indicate that the synthesized nanomaterial effectively mitigates corrosion of mild steel in 0.5 M HCl solution.

Keywords

Low-carbon steel corrosion; zinc acetate; omeprazole; nanocomposite; inhibition efficiency

Introduction

Hydrochloric acid solutions are widely utilized in industrial operations such as acid pickling, boiler cleaning, oil well acidizing, ore processing, petrochemical production, and acid descaling. However, their highly aggressive nature often leads to severe corrosion of equipment and infrastructure [1]. Corrosion, which results in the gradual deterioration of materials, especially metals and alloys used across virtually all industries, remains a significant global challenge [2,3]. Several strategies have been developed to mitigate corrosion, including modification of process fluids, use of improved materials, and application of chemical inhibitors [4,5]. Among these approaches, corrosion inhibitors are regarded as one of the most effective and economically viable methods for reducing metal degradation in corrosive environments [6]. Their practical application in industry has made them a preferred choice for corrosion control [4]. The use of inhibitors is important for enhancing the service life of industrial infrastructure such as pipelines, storage vessels, and acid-cleaning equipment, especially in environments prone to rapid degradation and high maintenance costs [7]. Nevertheless, the use of conventional inhibitors such as zinc chromate has been restricted due to toxicity and environmental concerns, despite its excellent performance. Similarly, zinc phosphate pigments exhibit relatively poor inhibition efficiency due to their slight solubility in water, thereby necessitating the development of safer and more effective alternatives.

In recent years, multi-component inhibitor systems containing heteroatoms [8] such as nitrogen, phosphorus, and sulphur have gained attention as commercially available corrosion inhibitors [9]. Although these systems demonstrate good performance in aggressive environments, their synthesis is often complex and challenging. Consequently, the development of composite materials has emerged as a simpler and more efficient strategy for designing high-performance corrosion inhibitors. In particular, inorganic-organic nanocomposites have been extensively investigated due to their enhanced protective properties. For example, Umoren *et al.* (2022) [9] synthesized a chitosan-copper oxide nanocomposite *via* an *in situ* approach using olive leaf extract as a reducing agent. The resulting material, with varying chitosan contents (0.5 to 2.0 g), exhibited excellent inhibitory performance against X60 carbon steel in 5 wt.% HCl solution. These findings highlight the potential of such nanocomposites as effective corrosion inhibitors [9].

Well-engineered nanocomposites are increasingly recognized as promising materials for corrosion protection [10,11], particularly in coatings for metals and alloys. They can provide not only physical barrier protection but also advanced functionalities such as self-healing and stimulus-responsive behaviour. These coatings are typically produced using a wide range of matrix-reinforcement combinations that often act synergistically to enhance performance [12]. The rapid advancement of nanotechnology has further accelerated the development of innovative corrosion protection materials [1,13]. By manipulating matter at the nanoscale [14,15], significant improvements in physical, chemical, mechanical, and optical properties can be achieved [16]. This has enabled the design of materials with tailored physicochemical characteristics suitable for specific industrial applications [1,17]. In particular, inorganic-organic nanocomposites combine the desirable attributes of both components: high surface area, mechanical strength, and thermal stability of inorganic nanoparticles, along with the adsorption capability and functional flexibility of organic molecules. The synergistic interaction between these components often results in superior inhibition efficiency, improved surface coverage, and enhanced resistance to aggressive media.

Recent studies further demonstrate the effectiveness of nanocomposite-based inhibitors. For instance, $NiZn_2O_4$/epoxy nanocomposites have been reported to provide stable and efficient corrosion protection for mild steel in 1 M HCl, with performance dependent on concentration and

exposure time [18]. Similarly, ZnO/arginine/tyrosine nanocomposite has shown excellent inhibition properties in acidic environments [19]. Building on these advancements, the present study focuses on the synthesis and evaluation of a zinc acetate-omeprazole inorganic-organic nanomaterial as a corrosion inhibitor for mild steel in 0.5 M HCl solution. The chemical structure of omeprazole (Figure 1a) features several reactive sites, including nitrogen, oxygen, sulphur, and π electrons, which serve as robust anchoring points for the metal substrate. Zinc ions from zinc acetate (Figure 1b) have the potential to interact with water and oxygen to generate a compact, insoluble, and adherent passive film, such as $Zn(OH)_2$ or ZnO, on the metal surface. This layer could function as a physical barrier, thereby limiting the penetration of corrosive agents. The acetate moiety readily dissolves in aqueous media and can synergistically enhance the protective absorption characteristics of other organic compounds, including omeprazole, on the metal surface.

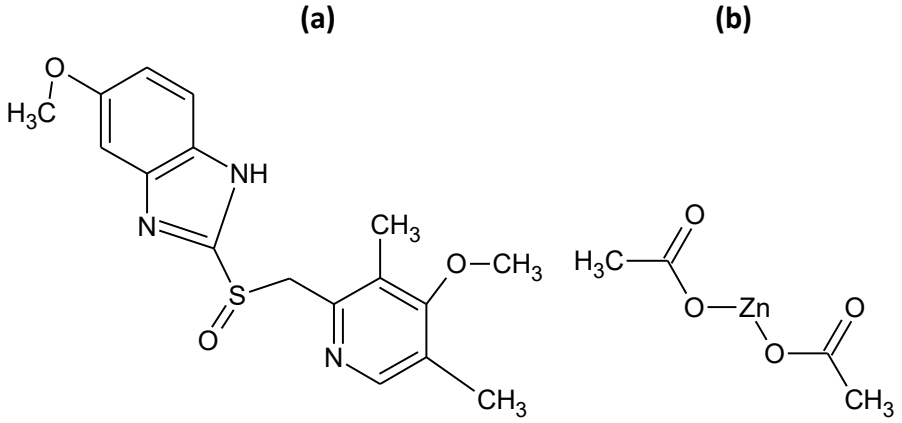

Figure 1. *Chemical structure of (a) omeprazole and (b) zinc acetate*

Experimental

Preparation of the nanomaterial

Aqueous ammonia was added gradually to an aqueous mixture containing 100 mL of 1 M zinc acetate and 50 mL of 0.5 g L^{-1} omeprazole. This mixture was then subjected to vigorous agitation and heated to 70 °C for 30 minutes, followed by sonication for 20 minutes. The resultant precipitate was processed through centrifugation and subsequently washed with water and ethanol. The isolated product was dried in an oven at 70 °C for 5 hours. Finally, the prepared material (ZO) was placed into bottles for subsequent characterization and corrosion assessment.

Characterization

X-ray diffraction (XRD) analysis was carried out using a Rigaku Miniflex 600 powder diffractometer (Rigaku Corporation, Japan), operated at 45 kV and 40 mA. The particle size distribution and polydispersity index (PDI) of the synthesized nanomaterial were determined using a Zetasizer (Zen1600, Malvern Instruments Ltd.). Deionized water, with a refractive index of 1.330, was used as the dispersing medium. Measurements were performed at 25 °C for 60 s using disposable cuvettes, with data collected at a measurement position of 4.65 mm. The recorded count rate was 395,600 counts *per* second.

Fourier transform infrared (FTIR) spectroscopy was conducted using a Cary 630 spectrometer (Agilent Technologies Inc.) over a wavenumber range of 4000 to 400 cm^{-1} to identify functional groups present in the nanomaterial. The morphology and structural features of the nanomaterial were examined using transmission electron microscopy (TEM).

Electrochemical tests

Electrochemical experiments were performed in a 0.5 M HCl solution, which served as the corrosive electrolyte. To ensure system stability and minimize capacitive effects, the open circuit potential (OCP) was monitored for 1800 seconds (30 minutes), allowing the system to reach a steady-state potential corresponding to the corrosion potential (E_{corr}). Subsequent electrochemical measurements were conducted under stabilized OCP conditions.

A conventional three-electrode cell configuration was employed, consisting of a platinum (Pt) wire as the counter electrode, mild steel as the working electrode, and an Ag/AgCl electrode as the reference. The Pt wire completed the electrical circuit and facilitated current flow, while the Ag/AgCl electrode provided a stable and reproducible reference potential due to its non-polarizable nature.

Electrochemical impedance spectroscopy (EIS) measurements were performed using an AC perturbation amplitude of 10 mV over a frequency (f) range of 100 kHz to 10 mHz. Potentiodynamic polarization studies were carried out at a scan rate of 0.2 mV s^{-1} over a potential range relative to the OCP. Measurements were conducted in the presence and absence of ZO. The concentration of ZO employed in this study was 0.1, 0.2 and 0.4 g L^{-1}. The obtained data were analysed using specialized electrochemical software: ZsimpWin (version 3.2) for EIS [13], employing appropriate equivalent circuit modelling, and EC-Lab software for polarization data analysis [13]. The inhibition efficiency (IE) and surface coverage were computed using the equations presented in a previous study [5].

Results and discussion

Transmission electron microscopy

Transmission electron microscopy (TEM) images provide comprehensive insights into the morphological and dimensional properties of the synthesized nanomaterial. Analysis of the micrographs presented in Figure 2 reveals that the particles predominantly exhibit a spherical [20,21] to near-spherical morphology, characterized by relatively smooth and well-defined edges.

This observation indicates that particle nucleation and subsequent growth were carried out in a manner that was both controlled and uniform. In various areas of the micrographs, the nanoparticles are distinctly separated; however, some regions exhibit minor aggregation, a phenomenon often associated with ultrafine particles owing to their high surface energy. The observed contrast in the images supports the conclusion that the material consists of discrete nanoscale particles rather than bulk structures, thereby affirming the efficacy of the synthesis method used to produce nanometre-sized entities. Quantitative analysis of particle sizes derived from TEM images indicates a range of 2.70 to 6.37 nm. A considerable fraction of the particles is concentrated within a narrower range of approximately 3-5 nm, suggesting a relatively uniform size distribution [22]. These diminutive particle sizes result in a high surface-to-volume ratio, which is beneficial for various applications that rely on surface interactions, such as catalysis, adsorption, and corrosion resistance. The images show no oversized particles, indicating that the synthesis conditions effectively curtailed excessive particle growth, thereby keeping the particles within the nanoscale range.

However, despite their nanoscale characteristics, the TEM images reveal some degree of particle agglomeration. The observed clustered structures appear to consist of loosely associated individual nanoparticles as opposed to fused or sintered aggregates. Such behaviour is commonly observed in nanocomposite systems, especially when the stabilizing or capping agents are inadequate to completely inhibit interparticle interactions.

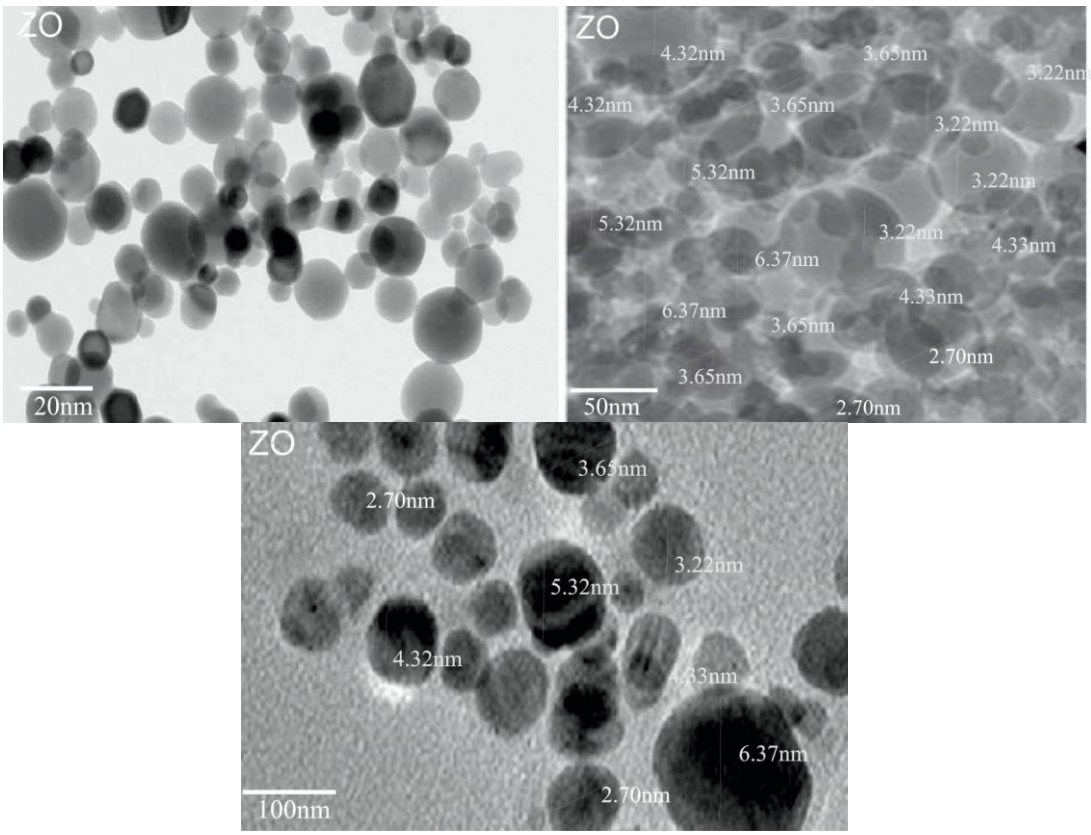

Figure 2. *TEM images of the synthesized ZO nanomaterial*

Dynamic light scattering

Dynamic light scattering (DLS) measurements offer valuable insight into the size distribution of nanomaterials in a dispersed phase [23]. The intensity-based size distribution profile derived from DLS, shown in Figure 3, is broad and exhibits multiple peaks, indicating polydispersity.

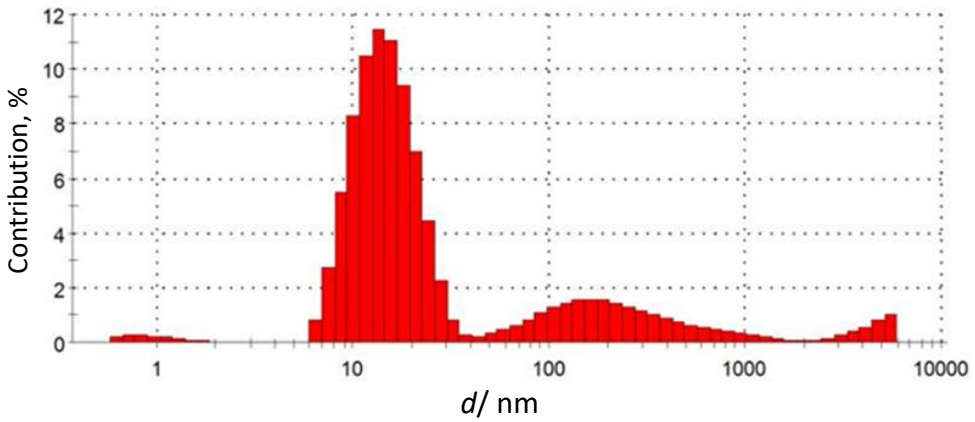

Figure 3. *Size distribution by DLS intensity of the synthesized ZO nanomaterial*

The predominant peak is found within the approximate range of 10-20 nm, reflecting the hydrodynamic diameter of the nanoparticles in suspension. This hydrodynamic size typically exceeds the core size obtained from TEM, as it accounts not only for the nanoparticle itself but also includes the surrounding solvent layer and any molecules adsorbed to the particle surface. Therefore, the observed enlargement in particle size from DLS data compared to TEM measurements is anticipated and further corroborates the presence of nanoscale particles. The mean hydrodynamic diameter (Z-average) of 59.79 nm indicates that the particles are primarily in the nanoscale range, thereby validating the successful synthesis of the material [13]. It is important

to note that the Z-average value, being intensity-weighted, is affected by the presence of larger particles or aggregates within the sample. The polydispersity index (PDI) of 0.249 indicates a moderately narrow size distribution. Generally, PDI values below 0.3 are viewed as indicative of acceptable uniformity in nanomaterials, suggesting that the sample exhibits a relatively homogeneous character, albeit not strictly monodisperse. This degree of dispersity is characteristic of inorganic-organic nanomaterials produced through conventional synthesis methods.

Alongside the predominant size distribution, the DLS profile reveals secondary peaks corresponding to considerably larger sizes, particularly exceeding 100 nm and reaching into the submicron range. These characteristics suggest the presence of particle aggregates within the suspension. Due to the pronounced sensitivity of DLS measurements to larger particles attributable to the intensity-dependent nature of light scattering, even a minor presence of aggregates can significantly skew the overall particle size distribution. Consequently, the identification of these larger size fractions implies that while the primary nanoparticles are relatively diminutive, they tend to form clusters within the liquid medium. This finding is consistent with the agglomeration patterns observed in TEM images, highlighting instability or interparticle interactions within the dispersion.

A direct comparison of the TEM and DLS results highlights the distinction between the actual particle core size and the hydrodynamic diameter of the nanomaterial. While TEM confirms that the primary particles are extremely small, ranging from 2.70 to 6.37 nm, DLS indicates significantly larger apparent sizes due to aggregation effects and the contribution of the surrounding solvation layer. Such differences between the two techniques are well recognized in nanomaterial characterization and arise from their fundamentally different measurement principles [24]. Several researchers have reported similar observations of significantly larger sizes measured by DLS than by TEM [25,26]. TEM provides information on the physical dimensions of dried particles, whereas DLS reflects the effective size of particles in a dispersed environment, including interparticle interactions and surface-bound species.

X-ray diffraction

The X-ray diffraction (XRD) pattern (Figure 4) of the synthesized ZO nanomaterial reveals distinct diffraction peaks superimposed on a broad background, signifying the coexistence of both crystalline and amorphous phases [20].

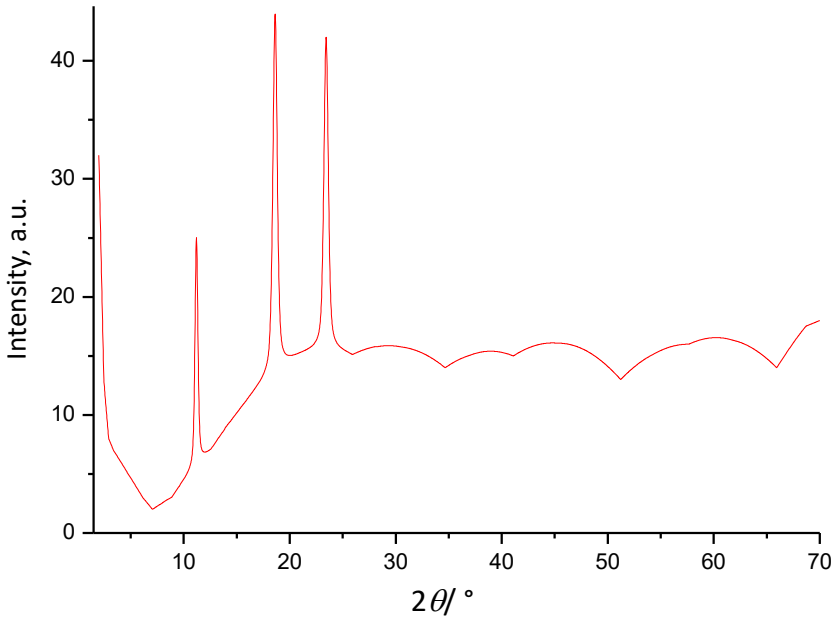

Figure 4. *XRD spectrum of the synthesized ZO nanomaterial*

The observed reflections within the range of $2\theta \approx$ 18 to 22°, in conjunction with weaker peaks noted at elevated diffraction angles, signify the crystalline characteristics of the metallic phase. A combination of a zinc salt and aqueous ammonia has been shown to yield ZnO nanoparticles, typically as a precipitate [27]. The presence of omeprazole may serve as a structural stabilizing agent within this process. However, incorporating pharmaceutical-grade omeprazole may introduce complex organic moieties, including S- and N-containing species, into the precursor mixture. These species may disrupt the nucleation and crystalline development of the ZnO lattice, leading to the formation of amorphous byproducts rather than pure ZnO. Nevertheless, these organic moieties can be advantageous for corrosion inhibition, as they create sites for interaction with the metal surface. The peaks within the range of $2\theta \approx$ 18 to 22° may be due to some disrupted lattice planes in ZnO owing to the presence of omeprazole, or incomplete phase formation. The first three prominent peaks suggest disrupted planes in ZnO: (100), (002), and (101) [27]. A broadening of the diffraction peaks is evident in the diffractogram, a phenomenon typical of materials with very small crystallite sizes. Also, the relatively low peak intensities suggest insufficient long-range crystalline order, a characteristic commonly associated with nanoparticles stabilized by organic molecules.

The presence of a broad hump in the low-angle region further suggests an amorphous phase, likely attributable to the omeprazole component. The absence of well-defined crystalline peaks characteristic of pure omeprazole suggests that the drug is either molecularly dispersed or present in an amorphous state within the matrix. This amorphous characteristic is advantageous for improving reactivity and surface interactions, which are crucial for applications such as corrosion inhibition and drug delivery. Minor shifts in peak positions, along with variations in peak intensities, may indicate lattice distortion or surface strain resulting from interactions between the metal nanoparticles and omeprazole molecules. Such phenomena are frequently observed in nanocomposite systems where organic molecules serve as stabilizing or capping agents, thereby affecting the structural properties of the nanoparticles.

Fourier transform infrared spectroscopy

The Fourier transform infrared (FTIR) spectrum of omeprazole (Figure 5a) displayed several characteristic absorption bands that align with the functional groups existing within the molecule. The peak at 3235.33 cm^{-1} could be attributed to the N-H stretching vibration associated with the benzimidazole moiety, whereas the absorption at 2922.23 cm^{-1} could be linked to the aliphatic C-H stretching stemming from the methyl and methoxy groups. The subtle signal observed at 2624.05 cm^{-1} may be associated with hydrogen-bonded N-H vibrations. A prominent absorption peak identified at 1714.58 cm^{-1} may be correlated with C=N stretching as well as the aromatic skeletal vibrations of the benzimidazole ring structure. The band observed at 1558.03 cm^{-1} corresponds to aromatic C=C stretching, while the absorption peak at 1446.21 cm^{-1} could be attributed to bending vibrations of the methyl group. Moreover, the absorption bands at 1386.57 and 1267.29 cm^{-1} signified C-N stretching and aryl methoxy (Ar-O-CH_3) stretching vibrations, respectively. The distinctive peak observed at 1013.84 cm^{-1} corresponds to the S=O stretching vibration associated with the sulfoxide group, an essential structural characteristic of omeprazole. The bands identified at 738.01 cm^{-1} and 670.92 cm^{-1} may be due to out-of-plane bending modes of aromatic C-H bonds, thereby reinforcing the aromatic nature of the compound.

The FTIR spectrum of the synthesized ZO nanomaterial presented in Figure 5b provides significant information regarding the functional groups present. A broad band identified around 3285 cm^{-1} is attributed to N-H and/or O-H stretching vibrations, signifying the presence of hydrogen bonding and

functional groups in omeprazole [2,20,26,28]. The spectral data indicate that these groups may interact with the surface of nanoparticles. A weak band identified around 2113 cm^{-1} is likely due to overtone or combination vibrations. The notable peak at approximately 1543 cm^{-1} is attributed to C=N stretching vibrations and/or aromatic ring modes, indicative of the benzimidazole structure in omeprazole. Additional absorption bands detected at 1448 cm^{-1} and 1409 cm^{-1} correspond to aromatic C=C stretching [2,29] and CH_2 bending vibrations.

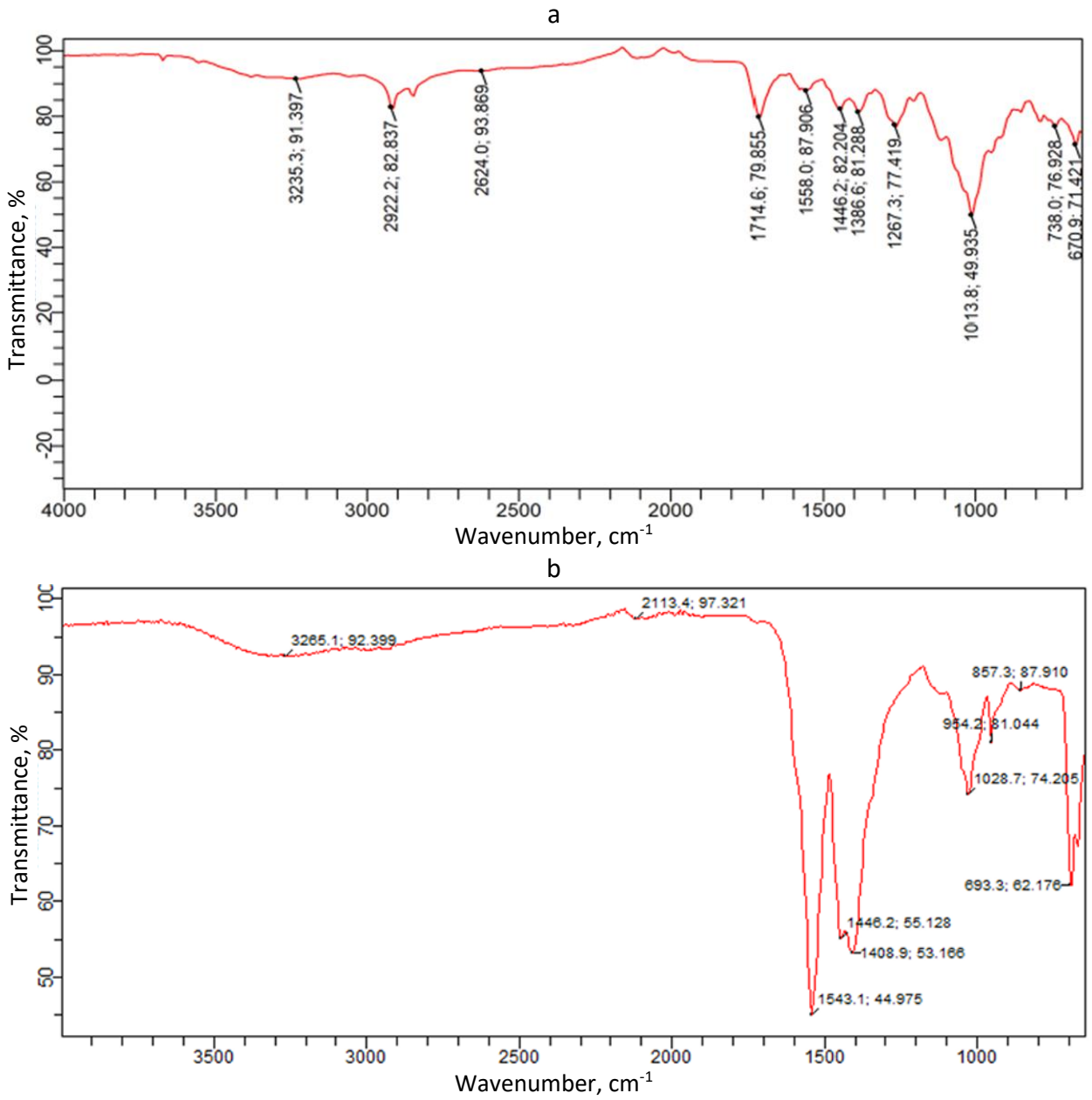

***Figure 5**. FTIR spectrum of a - omeprazole and b - synthesized ZO nanomaterial*

The robust peak observed near 1028 cm^{-1} is attributed to C-O-C ether linkages and/or S=O stretching vibrations, both of which are significant functional groups in omeprazole. Moreover, bands occurring in the range of 954-693 cm^{-1} are associated with out-of-plane bending vibrations of aromatic C-H bonds, further substantiating the presence of the drug molecule within the nanocomposite. The band near 650 cm^{-1} could be attributed to Zn-O stretching vibration. Comparison with the spectrum of pure omeprazole reveals noticeable shifts in peak positions and variations in intensity, indicating strong interactions between the drug's functional groups and the metal surface. These changes

suggest that heteroatoms such as nitrogen, oxygen, and sulphur serve as coordination centres, donating electron density to the metal and facilitating the formation of a protective adsorption layer. This type of interaction is widely recognized in drug-metal nanocomposites and typically involves coordination bonding rather than the formation of new covalent bonds.

The FTIR spectrum of zinc acetate exhibits several notable absorption bands resulting from the vibrational modes of the acetate ion, as well as, in the case of hydrated zinc acetate, the water molecules that are coordinated with it. A broad absorption band present in the range of 3200 to 3600 cm^{-1} is linked to the O-H stretching vibrations of the water molecules found in zinc acetate dihydrate. Weak absorption bands located between 2900 and 3000 cm^{-1} correspond to the C-H stretching vibrations associated with the methyl groups of the acetate ions. A critical feature of the spectrum is a pronounced absorption band between 1550 and 1600 cm^{-1}, attributed to asymmetric stretching vibrations of the carboxylate group. A significant band appears within the range of 1400 to 1450 cm^{-1}, which is associated with the symmetric stretching vibrations of the carboxylate group. Additional absorption bands observed around 1340-1360 cm^{-1} can be attributed to methyl group bending vibrations. The maxima observed in the range of 1000 to 1100 cm^{-1} are ascribed to the C-C stretching and C-H rocking vibrations of the acetate ion. In the lower-wavenumber spectrum, the bands observed between 400 and 600 cm^{-1} are attributed to Zn-O stretching vibrations, thereby providing evidence of the interaction between zinc ions and the oxygen atoms in the acetate groups [30].

Open circuit potential

The open circuit potential (OCP) curves in Figure 6 provide important insights into the interfacial characteristics of mild steel immersed in 0.5 M HCl, both in the absence and presence of ZO at various concentrations.

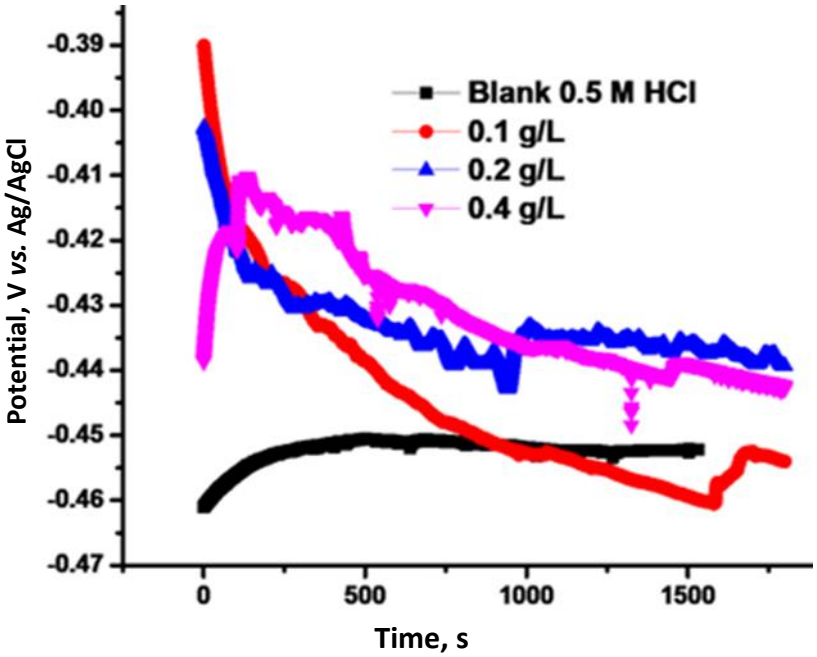

Figure 6. *OCP profiles of mild steel for blank uninhibited system in comparison with different concentrations of ZO inhibitor in 0.5 M HCl*

In the uninhibited solution, the OCP stabilizes at more negative potentials (~ -0.46 V *vs.* Ag/AgCl), indicating ongoing corrosion and continuous dissolution of the metal in the acidic medium. Upon the addition of ZO, a noticeable shift in potential toward more positive (noble) values occurs [20], particularly at ZO concentrations of 0.2 and 0.4 g L^{-1}. This shift might be due to the adsorption of ZO

molecules onto the steel surface, forming a protective layer that mitigates anodic dissolution [31]. Given that the observed potential displacement is relatively modest (generally below 85 mV), ZO cannot be distinctly categorized as solely anodic or cathodic; instead, it functions as a mixed-type inhibitor. The initial fluctuations noted during shorter immersion times can be ascribed to dynamic adsorption-desorption phenomena and surface restructuring processes, after which the potential stabilizes, suggesting the formation of a relatively stable protective film. The enhanced stability of the potential with increasing inhibitor concentration indicates improved surface coverage and superior corrosion protection.

Potentiodynamic polarization

The results from potentiodynamic polarization (Tafel) corroborate the observations from OCP analysis, offering quantitative insights into the inhibition mechanism. The Tafel plots are presented in Figure 7.

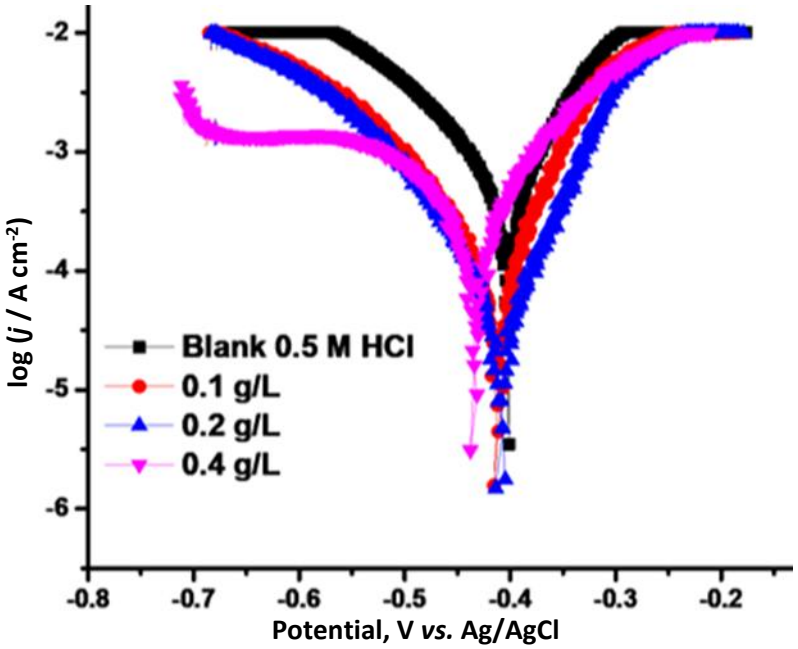

Figure 7. *PDP plots relating to mild steel for blank uninhibited system in comparison with different concentrations of ZO inhibitor in 0.5 M HCl*

The blank solution exhibits significantly higher corrosion current densities (Table 1), underscoring the rapid corrosion that occurs in the absence of protective agents [32]. However, the introduction of the inhibitor results in a notable decrease in corrosion current density (j_{corr}), with this effect becoming increasingly pronounced as the ZO concentration escalates, thereby indicating improved inhibition efficacy [33].

Table 1. *PDP parameters relating to mild steel for blank uninhibited system in comparison with different concentrations of ZO inhibitor in 0.5 M HCl*

ZO dosage, g L^{-1}	E_{corr} / mV *vs.* Ag/AgCl	j_{corr} / µAcm^{-2}	β_a / mVdec^{-1}	β_c / mVdec^{-1}	Surface coverage	IE, %
0.0 (blank)	-400	1781	53	198	-	-
0.1	-405	1315	54	170	0.262	26.2
0.2	-408	980	61	188	0.450	45.0
0.4	-450	461	78	176	0.741	74.1

This observation agrees with other reports [34]. Both the anodic and cathodic segments of the polarization curves are diminished in the presence of ZO, indicating that ZO effectively slows both

metal dissolution and the hydrogen evolution reaction [35]. The slight alterations in corrosion potential, E_{corr} less than 85 mV, are consistent with the OCP data, further validating the characterization of the inhibitor as a mixed-type [19,20,36]. Alterations in the anodic (β_a) and cathodic (β_c) Tafel slopes further indicate that the inhibitor impacts the kinetics of the electrochemical reactions [37], likely through its adsorption at active sites and the impediment of charge transfer. That is, the variations noted in both β_a and β_c suggest that the inhibitor molecules adsorbed onto the metal surface, thereby affecting both the anodic and cathodic reactions [38].

The parameters derived from PDP further substantiate the inhibitor's efficacy in reducing corrosion. In the absence of the inhibitor, the system exhibits a high corrosion current density (j_{corr} = 1781 µA cm^{-2}), indicating significant metal dissolution. However, with the introduction of the inhibitor, j_{corr} decreases sequentially to 1315, 980 and 461 µA cm^{-2} at concentrations of 0.1, 0.2 and 0.4 g L^{-1}, respectively, indicating a marked reduction in the corrosion rate [39,40]. In tandem, the inhibition efficiency rises from 26.2 to 74.1 %, underscoring the enhanced protective effect associated with increased dosages of ZO. At the highest concentration of 0.4 g L^{-1}, the most pronounced reduction in current density is observed, suggesting the development of a more compact and adherent protective film. The corrosion potential values exhibit only minor variations from the blank, particularly at lower concentrations, which implies a predominantly mixed-type inhibition with a slight inclination toward cathodic behaviour at elevated concentrations. The observed increase in surface coverage with increasing ZO concentration supports the formation of a protective adsorbed layer and is consistent with a previous study [19].

Electrochemical impedance spectroscopy

The electrochemical impedance spectroscopy (EIS) data, illustrated in Nyquist plots (Figure 8), complement the polarization findings and provide a deeper understanding of the corrosion mechanisms involved.

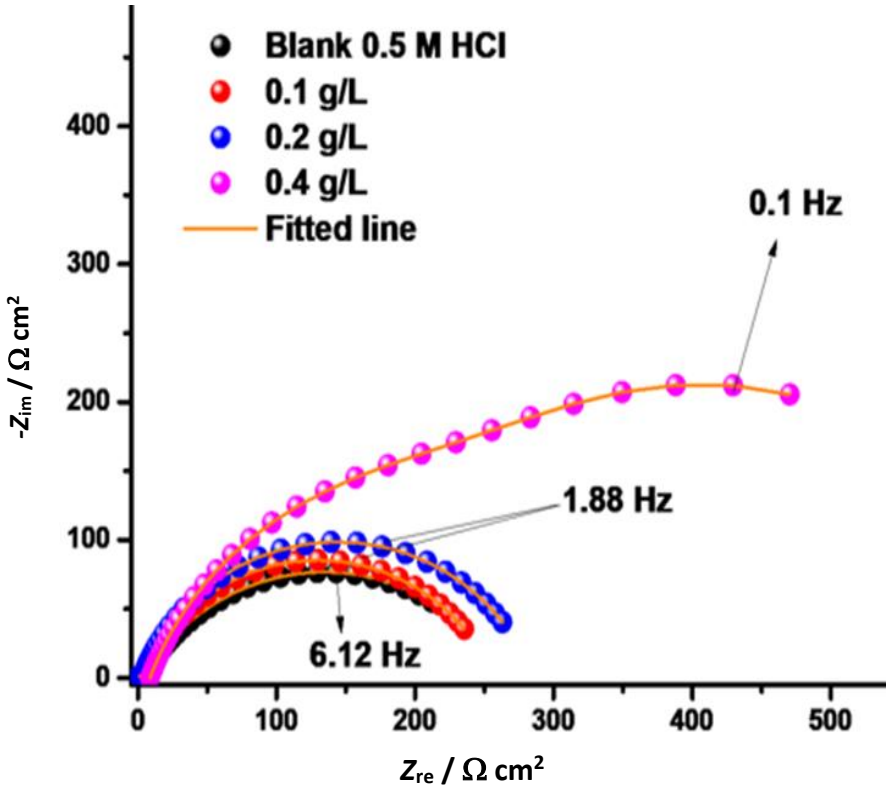

Figure 8. *Nyquist plots for EIS analysis of mild steel for blank uninhibited system in comparison with different concentrations of ZO in 0.5 M HCl*

Table 2. *EIS data relating to mild steel for blank uninhibited system in comparison with the different concentrations of ZO inhibitor in 0.5 M HCl*

ZO dosage, g L^{-1}	R_s / Ω cm^2	R_{po} / Ω cm^2	Q_1 / 10^{-5} $Ω^{-1}$ s^n cm^{-2}	n_1	R_{ct} / Ω cm^2	Q_2/ 10^{-5} $Ω^{-1}$ $s^n cm^{-2}$	n_2	Surface coverage	IE, %
0.0 (blank)	19.22	15.3	44.77	0.84	210.21	10.11	0.79	-	-
0.1	18.00	20.7	40.00	0.77	230.0	14.4	0.81	0.086	8.6
0.2	18.02	15.4	38.3	0.86	320.0	13.2	0.86	0.343	34.3
0.4	18.03	34.6	34.2	0.93	938.0	9.1	0.97	0.776	77.6

The Nyquist plots reveal depressed semicircles across all systems, indicative of charge-transfer-controlled processes on a heterogeneous surface [41,42]. The depressed nature of the semicircles reflects deviations from ideal capacitive behaviour due to surface irregularities. A marked increase in the diameter of these semicircles with rising inhibitor concentration is noted, signalling enhanced charge transfer resistance (R_{ct}) and improved corrosion resistance [43,44]. While the blank system exhibits a relatively small semicircle, the inhibited systems, particularly at 0.4 g L^{-1}, show significantly larger semicircles, confirming the development of an effective protective film.

More support is provided by the fitted EIS parameters (Table 2). The electrical equivalent circuit used to fit EIS data is shown in Figure 9. The solution resistance (R_s) remains nearly unchanged across all systems, indicating that the inhibitor has minimal influence on the electrolyte conductivity. In contrast, both pore resistance (R_{po}) and charge transfer resistance (R_{ct}) increase significantly, from 15.3 and 210.21 Ω cm^2 in the blank to 34.6 and 938.0 Ω cm^2 at 0.4 g L^{-1}, respectively. This marked increase in R_{ct} is associated with the formation of an adsorbed protective film that hinders electron transfer and slows down corrosion reactions. The values of parameter Q from CPE decrease with increasing inhibitor concentration, while the corresponding exponent (n) approaches unity, indicating a shift toward more ideal capacitive behaviour and a smoother and more homogeneous surface. The inhibition efficiency obtained from EIS reaches up to 77.6 % at 0.4 g L^{-1}, consistent with the PDP results and confirming the reliability of the electrochemical measurements. The discrepancies between the surface coverage and inhibition efficiency values obtained from EIS and PDP stem from the distinct methodologies used by each technique to assess the corrosion system.

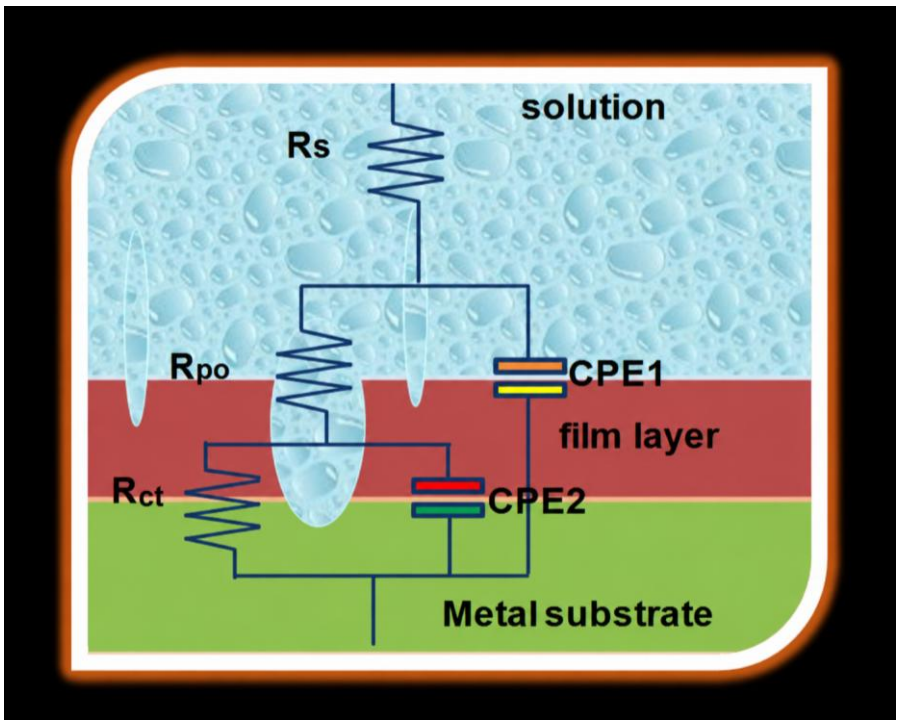

Figure 9*. Electrical equivalent circuit employed for fitting EIS data*

The Bode plots shown in Figure 10(a) and (b) offer valuable information on the corrosion performance of mild steel in 0.5 M HCl, both in the absence and presence of the inhibitor at concentrations ranging from 0.1 to 0.4 g L^{-1}.

The Bode modulus plot (log $|Z|$ *vs.* log f) demonstrates that the impedance response is strongly influenced by both frequency and ZO concentration [38]. In the blank solution, relatively low impedance values are observed across the entire frequency spectrum, indicating fast charge-transfer kinetics and minimal corrosion resistance. With the introduction of ZO, impedance increases markedly, especially at lower frequencies, a trend commonly linked to improved corrosion protection. This enhancement in $|Z|$ at low frequencies becomes more pronounced as the inhibitor concentration increases, with the 0.4 g L^{-1} system showing the highest impedance response [45]. Such behaviour suggests the development of a protective layer on the mild steel surface that restricts electrochemical reactions responsible for corrosion [38]. The near-linear trend in the mid-frequency region reflects capacitive characteristics typical of a charge-transfer-controlled process at the metal-electrolyte interface.

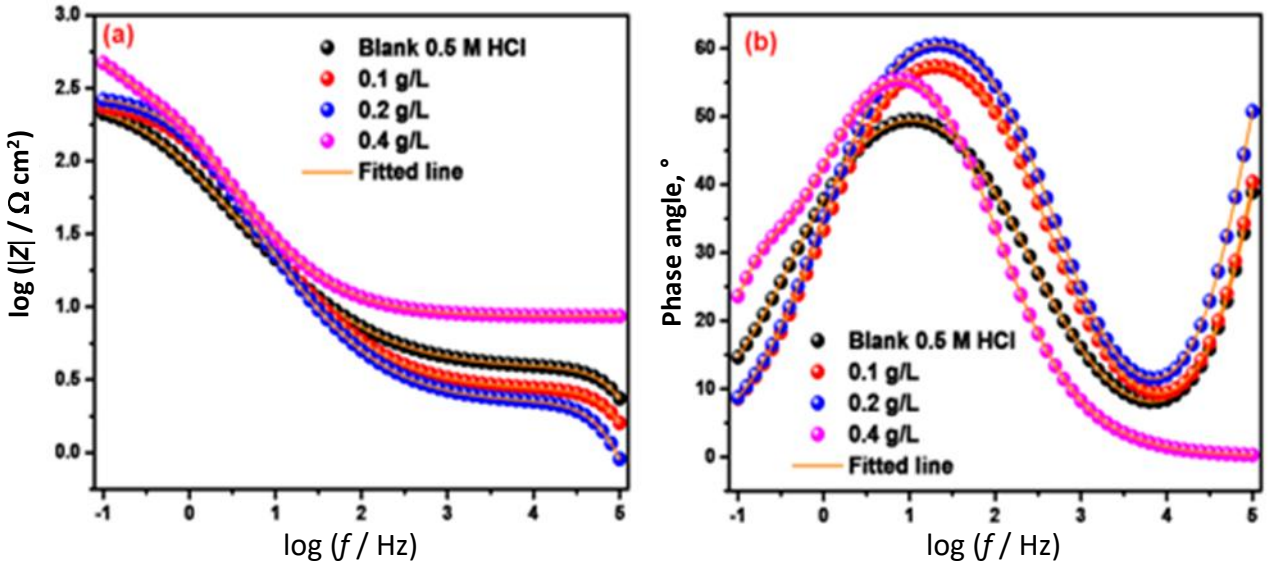

Figure 10. *Bode plots: (a) modulus and (b) phase angle of mild steel for blank uninhibited system in comparison with different concentrations of ZO in 0.5 M HCl*

The phase angle plot (phase angle *vs.* log f) further corroborates these findings by revealing changes in interfacial properties due to inhibitor adsorption. In the absence of ZO, the phase angle peak is lower and broader, indicating non-ideal capacitive behaviour and surface irregularities associated with ongoing corrosion. Upon adding the inhibitor, the maximum phase angle increases and shifts slightly toward higher frequencies, particularly at concentrations up to 0.2 g L^{-1}, suggesting enhanced capacitive behaviour and the formation of a more uniform and protective surface film. This rise in phase angle indicates improved surface coverage. However, at the highest concentration (0.4 g L^{-1}), a slight reduction or broadening of the phase angle peak is noticeable, which may be attributed to the formation of a thicker but less uniform film, as well as the possible influence of diffusion processes or multilayer adsorption effects.

Note that some deviations in the high-frequency regions of Bode plots from the response predicted by the equivalent electrical circuit in Figure 9 are observed. Variations observed in the high-frequency regions of Bode plots may arise from factors such as unaccounted distributed elements, parasitic inductances, geometric inconsistencies, and artifacts associated with the measurement equipment.

Comparison of associated reports

Table 3 presents a comparative analysis of several studies involving corrosion inhibition utilizing ZO (*i.e.* the inhibitor employed in the present study) and inhibitors that are connected to ZO, such as omeprazole and zinc acetate, all assessed in various corrosive environments and across different metal substrates [3,7,33,35,43]. Although direct comparisons are complicated by differences in experimental parameters, such as the medium used, inhibitor concentrations, and the metals examined, a general assessment of their efficacy remains feasible.

Table 3. *Summary of findings from related studies compared to the present study*

Inhibitor	Inhibitor dosage	Medium	Metal/ alloy	Maximum IE, %	Method	Ref.
Zinc acetate-omeprazole nanomaterial	0.4 g L^{-1}	0.5 M HCl	Mild steel	77.6	EIS	Present study
Expired omeprazole	0.060 g L^{-1}	0.5 M H_2SO_4	Carbon steel	95	Weight loss	[43]
Expired omeprazole	0.8 g L^{-1}	1 M H_2SO_4	Mild steel	94.47	Weight loss	[3]
Omeprazole	60 ppm	1 M HCl	Mild steel	97.03	Weight loss	[33]
Expired omeprazole	900 ppm	0.5 M HNO_3	Copper	97.7	Weight loss	[7]
Urtica dioica	200 ppm	3.5% NaCl	Mild steel	45	PDP	[35]
Zinc acetate	200 ppm	3.5% NaCl	Mild steel	35	PDP	[35]
Zinc acetate- *Urtica dioica*	200 ppm	3.5% NaCl	Mild steel	92	PDP	[35]

In the current investigation, the highest inhibition efficiency was achieved when the nano-material was administered at a concentration of 0.4 g L^{-1} in a 0.5 M HCl solution for mild steel, yielding a peak inhibition efficiency of 77.6 %, as determined by EIS. While this efficiency is relatively moderate compared with certain other reported inhibitors, it remains significant given the low dosage used and the use of electrochemical methods, which are generally regarded as more accurate and sensitive than weight-loss techniques. This suggests that the ZO offers a moderate degree of corrosion resistance, although it does not attain the higher efficiencies observed in specific organic inhibitors. Studies examining expired omeprazole have revealed notably superior inhibition efficiencies under various conditions. For instance, a concentration of 60 mg L^{-1} in 0.5 M H_2SO_4 yielded an efficiency of 95 % on carbon steel [43], whereas 0.8 g L^{-1} in 1 M H_2SO_4 resulted in a 94.47 % efficiency on mild steel [3]. In another study, omeprazole (not expired) at 60 ppm in 1 M HCl achieved an even greater efficiency of 97.03 % [33]. These results consistently highlight the robust inhibitive capabilities of omeprazole-based systems, regardless of their freshness, which can be attributed to the presence of heteroatoms such as nitrogen, oxygen, and sulphur that enhance effective adsorption on the metal surface. The observed pattern is further substantiated by the exceptionally high efficiency of 97.7 % for expired omeprazole in a 0.5 M HNO_3 solution for copper, indicating its potential utility across various metals and in highly aggressive acidic environments [7].

A study reported the efficacy of *Urtica dioica*, zinc acetate, and their combination in mitigating mild steel corrosion in a 3.5 % NaCl solution [35]. The *Urtica dioica* extract exhibited a significantly lower inhibition efficiency of 45% in a 3.5% NaCl solution against mild steel, indicating its limited efficacy in chloride-rich environments. Zinc acetate demonstrated even less effectiveness, achieving only 35 % inhibition under identical conditions. Nevertheless, the combination of *Urtica dioica* and zinc acetate yielded a marked improvement, with the inhibition efficiency rising to 92 % [35]. This observation underscores a synergistic interaction between the organic extract and the inorganic salt, resulting in improved adsorption and the formation of a more protective film. A common observation across most related studies is the dominance of mixed-type inhibition mechanisms,

meaning that most inhibitors influence both the anodic dissolution of the metal and the cathodic hydrogen evolution simultaneously. In relation to the nanomaterial analysed in this study, these findings suggest that inhibitors derived from omeprazole and zinc acetate may provide good corrosion protection, especially when applied in optimal concentrations.

Conclusions

A zinc acetate-omeprazole (ZO) nanomaterial was synthesized and characterized. The particles of ZO (with sizes ranging from 2.70 to 6.37 nm) predominantly exhibited a spherical to near-spherical morphology and a Z-average diameter of 59.79 nm, signifying that the particles are primarily situated within the nanoscale range. XRD findings suggest the coexistence of both crystalline and amorphous phases in the prepared material. A progressive decline in corrosion current density was observed as inhibitor concentration increased. The nanomaterial exhibited a mixed-type inhibition mechanism rather than a purely anodic or cathodic one. The charge transfer resistance increased in the presence of the nanomaterial. The inhibition efficiency was found to increase with increasing ZO concentration. These findings indicate that the synthesized nanomaterial effectively mitigates corrosion of mild steel in 0.5 M HCl solution.

Acknowledgment: *We acknowledge the technical support of Dr. Vitalis Ikenna Chukwuike*

Funding: *This research received no grant from any funding agency.*

References

[1] V. Rajasekar, M. Shyamala, J. Aravind, Green, environmentally friendly synthesis of MnO nanoparticles for corrosion inhibition in mild steel, *Global NEST Journal* **26** (2024) 05891. https://doi.org/10.30955/gnj.005891

[2] S. A. Omogbehin, F. E. Olasehinde, M. A. Adebayo, M. J. Jabar, Synthesis and Characterization of Tectona Grandis Dye Nanoparticle as a Potential Inhibitor for Corrosion of Mild Steel in 1 M HCl Solution, *Progress in Chemical and Biochemical Research* **7** (2024) 323-344. https://doi.org/10.48309/PCBR.2024.449643.1345

[3] O. D. Onukwuli, I. J. Obibuenyi, L. Nnodi, U. L. Ezeamaku, J. O. Ezeugo, M. Omotioma, Investigating Inhibitory Actions of Expired Omeprazole in Sulphuric Acid as Corrosion Resistance of Mild-steel, *International Journal of Advanced Engineering and Management Research* **10** (2025) 175-199. http://dx.doi.org/10.51505/ijaemr.2025.1010

[4] U. R. Sharma, N. Sharma. Green Synthesis, Anti-cancer and Corrosion Inhibition Activity of Cr_2O_3 Nanoparticles, *Biointerface Research in Applied Chemistry* **11** (2021) 8402-8412. https://doi.org/10.33263/BRIAC111.84028412

[5] M. M. Mchihi, S. R. Ibukunola, B. O. Seriki, A. O. Eruola, A. T. Adejare, P. H. Ado, O. S. Olutunji, Influence of *Bauhinia tomentosa* Stem Bark Extract on the Electrochemical Behavior of Low-Carbon Steel in 1 M HCl, *Jordanian Journal of Engineering and Chemical Industries* **9** (2026) 77-89. https://doi.org/10.48103/jjeci962026

[6] N. W. Odozi, A. S. Adetoba, M. M. Mchihi, A. N. Akpaetok, *Synsepalum dulcificum* leaves extract as green inhibitor for mild steel corrosion in hydrochloric acid, *ChemSearch Journal* **12** (2021) 47-54. http://www.ajol.info/index.php/csj

[7] A. Farooq, E. H. Ali, Z. W. Ahmed, A. A. Khadom, K. F. Al-azawi, Expired omeprazole as an effective corrosion inhibitor for copper in nitric acid, *International Journal of Electrochemical Science* **21** (2026) 101303. https://doi.org/10.1016/j.ijoes.2026.101303

[8] F. Chioma, N. W. Odozi, M. M. Mchihi, M. A. Olatunde, Synthesis, spectroscopic, and density functional theory studies of the corrosion inhibitive behaviour of *n*-(1,4-dihydro-1,4-dioxo-

naphthalene-3-yl)pyrazine-2-carboxamide chelator-ligand, *Global Journal of Pure and Applied Sciences* **28** (2022) 39-50. https://dx.doi.org/10.4314/gjpas.v28i1.6

[9] P. S. Umoren, D. Kavaz, S. A. Umoren, Corrosion inhibition evaluation of chitosan-CuO nanocomposite for carbon steel in 5% HCl solution and effect of KI addition, *Sustainability* **14** (2022) 7981. https://doi.org/10.3390/su14137981

[10] M. Basik, M. Mobin, M. Shoeb, Cysteine-silver-gold nanocomposite as potential stable green corrosion inhibitor for mild steel under acidic condition, *Scientific Reports* **10** (2020) 279. https://doi.org/10.1038/s41598-019-57181-5

[11] T. Brindha, R. Rathinam, S. Dheenadhayalan, R. Sivakumar, Nanocomposite coatings in corrosion protection applications, *Oriental Journal Chemistry* **37** (2021) 1062-1067. https://doi.org/10.13005/ojc/370507

[12] L. M. Muresan, Nanocomposite coatings for anti-corrosion properties of metallic substrates, *Materials* **16** (2023) 5092. https://doi.org/10.3390/ma16145092

[13] M. M. Mchihi, N. W. Odozi, C. Nwafor, E. M. Okon-Okodi, F. O. Ayuba, ZnO nanoparticles functionalized with amoxicillin: Synthesis, characterization and assessment of corrosion inhibition performance of aluminum in alkaline medium, *Next Nanotechnology* **9** (2026) 100438. https://doi.org/10.1016/j.nxnano.2026.100438

[14] Z. Aalami, M. Hoseinzadeh, P. H. Manesh, A. H. Aalami, Z. Es'haghi, M. Darroudi, A. Sahebkar, H. A. Hosseini, Synthesis, characterization, and photocatalytic activities of green sol-gel ZnO nanoparticles using *Abelmoschus esculentus* and *Salvia officinalis*: A comparative study versus co-precipitation-synthesized nanoparticles, *Heliyon* **10** (2024) e24212. https://doi.org/10.1016/j.heliyon.2024.e24212

[15] N. W. Odozi, M. M. Mchihi, M. A. Olatunde, Review of recent advances in plant-mediated synthesis and applications of $3d^5$-$3d^{10}$ metal oxide nanoparticles and their composites, *Dutse Journal of Pure and Applied Sciences* **9** (2023) 91-120. https://dx.doi.org/10.4314/dujopas.v9i4b.10

[16] J. Santhoshkumar, S. Rajeshkumar, S. Venkat Kumar, Phyto-assisted synthesis, characterization and applications of gold nanoparticles – A review, *Biochemistry and Biophysics Reports* **11** (2017) 46-57. http://dx.doi.org/10.1016/j.bbrep.2017.06.004

[17] S. Mourdikoudis, R. M. Pallares, N. T. Thanh, Characterization techniques for nanoparticles: comparison and complementarity upon studying nanoparticle properties, *Nanoscale* **10** (2018) 12871. https://doi.org/10.1039/C8NR02278J

[18] Z. E. Kennedy, C. Sneha, P. Bijesh, M. Zakriya, V. Andal, S. Vaithilingam, Effect of $NiZn_2O_4$/epoxy nanocomposite as corrosion inhibitors on mild steel, *Discover Nano* **20** (2025) 182. https://doi.org/10.1186/s11671-025-04302-x

[19] M. M. Mchihi, A. M. Olatunde, N. W. Odozi, *Ficus sur* mediated synthesis of mesoporous ZnO nanoparticles and novel ZnO/Arginine/Tyrosine nanocomposite as eco-friendly corrosion inhibitors for mild steel in hydrochloric acid medium, *Moroccan Journal of Chemistry* **12** (2024) 1122-1152. https://doi.org/10.48317/IMIST.PRSM/morjchem-v12i3.42782

[20] A. O. Ezzat, V. S. Aigbodion, H. A. Al-Lohedana, C. J. Ozoudee, Unveiling the corrosion inhibition efficacy and stability of silver nanoparticles synthesized using *Anacardium occidentale* leaf extract for mild steel in a simulated seawater solution, *RSC Advances* **14** (2024) 18395. https://doi.org/10.1039/D4RA02362E

[21] S. Ashrafi-Saiedlou, M. H. Rasouli-Sadaghiani, M. Fattahi, Green synthesis of iron oxide nanoparticles using *Thymus migricus* for multifunctional applications in antioxidant, antimicrobial, photocatalytic, and seed priming processes, *Heliyon* **11** (2025) e42933. https://doi.org/10.1016/j.heliyon.2025.e42933

[22] M. Á. Aguilar-Méndez, T. Espinosa-Solares, F. Guerrero-Toledo, D. Canseco-González, A. Velázquez-Hernández, G. S. Aguilar-Moreno, E. Navarro-Cerón, Synthesis and

characterisation of magnetite nanoparticles using gelatin and starch as capping agents, *IET Nanobiotechnology* **14** (2020) 94-97. https://doi.org/10.1049/iet-nbt.2019.0204

[23] A. F. Osman, A. M. Abdallah, M. S. Bafawi, M. Roumie, R. Awad, Characterization of lead oxide milled nanoparticles and the effect of their incorporation on the thermal properties of polystyrene, *Journal of Engineering Science and Technology* **18** (2023) 481-507. https://jestec.taylors.edu.my/Vol%2018%20Issue%201%20February%20%202023/18_1_32.pdf

[24] J. B. Safari, V. S. Ushindi, F. C. Andema, P. M. Hamuli, E. B. Irenge, B. M. Vuangi, E. N. Zola, B. K. Baraka, C. M. Bilamirwa, V. M. Matabaro, F. P. Angbongbo, V. Nsabatien, J. Zanga, E. M. Metelo, R. W. Krause, A. Balčiūnaitienė, P. B. Memvanga, Plant-based synthesis of silver nanoparticles using aqueous leaf extracts of *Cinchona calisaya Wedd*. and *Cinchona pubescens Vahl*: physicochemical characterisation and biological activities, *Discover Nano* **20** (2025) 162. https://doi.org/10.1186/s11671-025-04326-3

[25] S. Alamdari, M. S. Ghamsari, C. Lee, W. Han, H. Park, M. J. Tafreshi, H. Afarideh M. H. Ara, Preparation and Characterization of Zinc Oxide Nanoparticles Using Leaf Extract of *Sambucus ebulus*, *Applied Sciences* **10** (2020) 3620. https://doi.org/10.3390/app10103620

[26] H. A. El Gizawy, R. H. Abd El-Aleam, N. H. Hassan, Green silver nanoparticles of Khaya senegalensis as dual inhibitors of viral thymidine kinase and 3 C protease: metabolomics, and computational insights, *Scientific Reports* **16** (2026) 10527. https://doi.org/10.1038/s41598-026-43691-6

[27] A. Nejabatdoust, A. Salehzadeh, H. Zamani, Z. Moradi-Shoeili, Synthesis, Characterization and Functionalization of ZnO Nanoparticles by Glutamic Acid (Glu) and Conjugation of ZnO@Glu by Thiosemicarbazide and Its Synergistic Activity with Ciprofloxacin Against Multi-drug Resistant *Staphylococcus aureus*, *Journal of Cluster Science* **30** (2019) 329-336. https://doi.org/10.1007/s10876-018-01487-3

[28] M. d. P. Marcos-Carrillo, N. -R. Checca-Huaman, E. C. Passamani, J. A. Ramos-Guivar, Biosynthesis and Characterization of Iron Oxide Nanoparticles Using *Chenopodium quinoa* Extract, *Nanomaterials* **14** (2024) 1607. https://doi.org/10.3390/nano14191607

[29] M. Kumar, R. Ranjan, M. S. Sinha, B. S. Raipat. Different techniques utilized for characterization of metallic nanoparticles synthesized using biological agents: A review, *Balneo and PRM Research Journal* **14** (2023) 534. https://doi.org/10.12680/balneo.2023.534

[30] Z. Luo, W. Cheng, H. Chen, X. Fu, X. Peng, F. Luo, L. Nie, Preparation and properties of enzyme-modified cassava starch-zinc complexes, *Journal of Agricultural and Food Chemistry* **61** (2013) 4631-4638. https://doi.org/10.1021/jf4016015

[31] M. M. Mchihi, N. W. Odozi, A. B. Odimuko. Deciphering properties of *Dryopteris marginalis* as green corrosion inhibitor for mild steel in HCl: Electrochemical, gas chromatography and DFT studies, *Sustainable Chemistry One World* **7** (2026) 100103. https://doi.org/10.1016/j.scowo.2025.100103

[32] M. M. Mchihi, A. M. Olatunde, N. W. Odozi. Electrochemical and Gravimetric Studies of the Corrosion Inhibitory Properties of Green Synthesized Copper Oxide Nanoparticles Mediated by *Ficus sur* for Mild Steel in HCl, *Jordan Journal of Chemistry* **20** (2025) 81-93. https://doi.org/10.47014/20.2.1

[33] Sudheer, M. A. Quraishi, Effect of pharmaceutically active compound Omeprazole, on the corrosion of mild steel in hydrochloric acid solution. *Journal of Chemical and Pharmaceutical Research* **3(5)** (2011) 82-92. https://www.jocpr.com/articles/effect-of-pharmaceutically-active-compound-omeprazole-on-thecorrosion-of-mild-steel-in-hydrochloric-acid-solution.pdf

[34] M. M. Mchihi, N. W. Odozi, S. A. Gbolahan, Electrochemical investigation of the inhibitory effect of zinc oxide nanoparticles/tenofovir disoproxil fumarate nanocomposite on mild steel corrosion in 1 M hydrochloric acid, *Analytical and Bioanalytical Electrochemistry* **16** (2024) 559-567. https://doi.org/10.22034/abec.2024.714079

[35] E. Salehi, R. Naderi, B. Ramezanzadeh, Synthesis and characterization of an effective organic/inorganic hybrid green corrosion inhibitive complex based on zinc acetate/Urtica Dioica, *Applied Surface Science* **396** (2017) 1499-1514. https://doi.org/10.1016/j.apsusc.2016.11.198

[36] N. C. Ngobiri, Y. Li, L. Liu. Corrosion inhibition and electrochemical behavior of commercial Rutin in an acidic environment, *Portugaliae Electrochimica Acta* **39** (2021) 323-334. https://doi.org/10.4152/pea.2021390502

[37] B. P. Maliekkal, J. T. Kakkassery, V. R. Palayoor, Efficacies of sodium nitrite and sodium citrate–zinc acetate mixture to inhibit steel rebar corrosion in simulated concrete interstitial solution contaminated with NaCl, *International Journal of Industrial Chemistry* **9** (2018) 105-114. https://doi.org/10.1007/s40090-018-0142-7

[38] K. Dahmani, Z. Aribou, O. Kharbouch, I. Saber, N. Er-rahmany, M. Galai, M. Rbaa, H. A. El-Serehy, A. Chaouiki, M. Touhami, M. Cherkaoui, Electrochemical and theoretical insight into the corrosion inhibition of brass by water-soluble organic compounds in 3% NaCl solution, *Journal of the Taiwan Institute of Chemical Engineers* **178** (2026) 106505. https://doi.org/10.1016/j.jtice.2025.106505

[39] N. W. Odozi, R. Saheed, M. M. Mchihi, Application of *peperomia pellucida* leaves extract as a green corrosion inhibitor for mild steel in 1.0 M hydrochloric acid solution, *ChemSearch Journal* **10** (2019) 88-93. http://www.ajol.info/index.php/csj

[40] M. M. Shaban, N. M. El Basiony, A. B. Radwan, E. E. El-Katori, A. Abu-Rayyan, N. H. Bahtiti, M. M. Abdou, Electrochemical investigation of C-Steel corrosion inhibition, in silico, and sulfate-reducing bacteria investigations using pyrazole derivatives, *ACS Omega* **8** (2023) 30068-30080. https://doi.org/10.1021/acsomega.3c02333

[41] M. Mahdavian, R. Naderi, Corrosion inhibition of mild steel in sodium chloride solution by some zinc complexes, *Corrosion Science* **53** (2011) 1194-1200. https://doi.org/10.1016/j.corsci.2010.12.013

[42] A. H. Ariffin, W. M. Nik, S. Abdullah, M. I. Isa, V. Izionworu, M. F. Zulkifli, Corrosion inhibition study of carboxymethyl cellulose-ionic liquid via electrochemical and machine learning technique, *Malaysian Journal of Analytical Sciences* **28** (2024) 265-276. https://mjas.analis.com.my/mjas/v28_n2/pdf/Ariffin_28_2_3.pdf

[43] L. E. Tsygankova, V. A. Bryksina, A. A. Uryadnikov, A. E. Abramov, Protective efficiency of expired drug against acid corrosion of carbon steel, *International Journal of Corrosion and Scale Inhibition* **11** (2022) 564-576. http://dx.doi.org/10.17675/2305-6894-2022-11-2-7

[44] M. M. Mchihi, N. W. Odozi, A.O. Nurudeen, M. C. Emesiani, B. O. Seriki. Assessment of Helianthus tuberosus leaves extract as eco-friendly corrosion inhibitor for Aluminum in sodium hydroxide: Insights from electrochemical, gravimetry and computational consideration, *Moroccan Journal of Chemistry* **12** (2024) 1462-1483. https://doi.org/10.48317/IMIST.PRSM/morjchem-v12i4.49160

[45] N. W. Odozi, M.C Emesiani, C. D. Charles, B. O. Seriki, M. M. Mchihi, Electrochemical studies of the corrosion inhibitory potential of *Annona muricata* leaves extract on aluminum in hydrochloric acid medium, *FUDMA Journal of Sciences* **8** (2024) 395-401. https://doi.org/10.33003/fjs-2024-0803-2460